Eumelanin-based multisensory platform: A case of study for photolithographic patterning

João V. Paulin [a,*], Luiz G.S. Albano [a], Davi H.S. Camargo [a], Mariane P. Pereira [a], Bruna A. Bregadiolli [b], Carlos F.O. Graeff [b,c], Carlos C.B. Bufon [a,c,d,*]

[a] Brazilian Nanotechnology National Laboratory (LNNano), Brazilian Center for Research in Energy and Materials (CNPEM), Campinas, SP 13083-970, Brazil
[b] School of Sciences, Department of Physics, São Paulo State University (UNESP), Bauru, SP 17033-360, Brazil
[c] School of Sciences, Postgraduate Program in Materials Science and Technology (POSMat), São Paulo State University (UNESP), Bauru, SP 17033-360, Brazil
[d] Mackenzie Presbyterian Institute, Mackenzie Institute for Research in Graphene and Nanotechnologies – MackGraphe, São Paulo, SP 01302-907, Brazil

ABSTRACT

Eumelanin, the most abundant brown-black pigment found in humans, is an ideal candidate for bioelectronics and eco-design technologies due to its biocompatibility, biodegradability, and hydration-dependent conductivity. Here, we validate the use of standard photolithography for integrating synthetic eumelanin into robust solid-state device platforms without unconventional methodologies. By combining AFM, Raman, and XPS with DC and AC electrical measurements, we have shown that eumelanin's film topography, chemical composition, and charge transport are not affected by the pattern process. Based on these findings, we explore interdigitated electrode structures for pH, humidity, and contact sensing system aiming at miniaturized wearable technologies for human healthcare monitoring.

1. Introduction

Eumelanin is a complex structural system composed of several units of 5,6-dihydroxyindole (DHI) and 5,6-dihydroxyindole-2-carboxylic acid (DHICA) in different oxidation states (Fig. 1(a)). As a black-brown natural pigment, it has inherent biocompatibility [1], potential biodegradability [2], and conductivity depending on the hydration [3–5] with solid-state protonic current [6–9], and device-quality thin-films processability [10,11]. These properties have allowed eumelanin to be tested in various devices platforms such as batteries [12,13], ion-to-electron transducers [14], pH sensors [15,16], supercapacitors [17,18], and UV-shielding [19]. The interaction of eumelanin with metal ions and metal oxides has also been of great interest for technological applications [20–24].

Among the mentioned applications, eumelanin-based films have predominantly been made by spin-coating or drop-cast techniques, which are not fully compatible with the current tendency towards smaller and portable devices. An unconventional and environmentally friendly lithography process based on Parylene-C patterning was the first attempt to miniaturize eumelanin-based devices [17]. In this

methodology, the desired patterns are made on the Parylene-C layer, and eumelanin is deposited on top of it. Additionally, although active areas of 0.08 cm^2 can be achieved, technological challenges would be expected during the peeled-off on active areas at a micrometer scale. Recently, a composite based on silk fibroin (as structural matrix) and natural eumelanin (in concentrations up to 28% (w/w), as the electroactive component) was patterned using photolithography [25]. Even though micro-architectures can be obtained, there will always be a silk contribution in the films, which may not be welcome, especially when smooth and homogeneous film surfaces are necessary. Natural silk and natural eumelanin can also have environmental impurities that are not desirable for reproducible and efficient devices [26].

Unlike the studies mentioned above, our intention with the present work is to extend the standard photolithography microfabrication processes to deterministically fabricate complex structures for (bio)electronics applications to synthetic eumelanin by itself. As a proof-of-concept for eumelanin patterning, we have evaluated the synthetic sulfonated-eumelanin. The advantages of the sulfonated-eumelanin over the standard and non-functionalized eumelanin are (i) the overall optical, electrochemical, and electrical thin-film properties remain, in
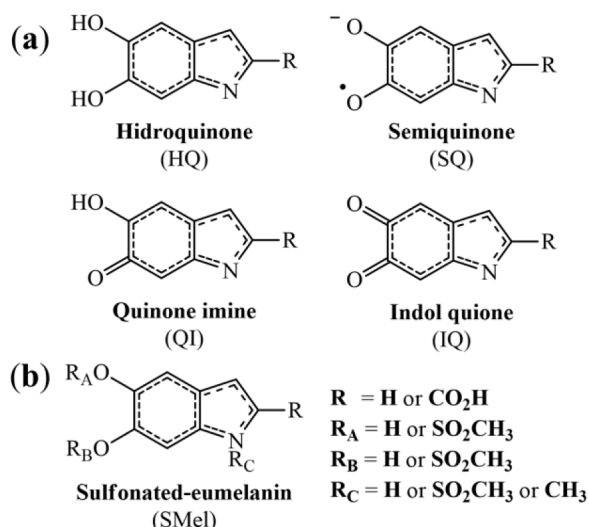
Fig. 1. (a) Different redox states of eumelanin's starting monomers. R = H for DHI species and R = COOH for DHICA. (b) Basic monomeric structure of sulfonated-eumelanin.

essence, unchanged even with the presence of sulfonated moieties attached to its indole structure (Fig. 1(b)) [9,11,27]; (ii) the biocompatibility of sulfonated-eumelanin is slightly better [28]; (iii) it can be solubilized in a broad range of solvents without the use of highly oxidative aqueous solutions [9,29], and; (iv) are not soluble in water [9, 29]. Our results indicate that the indole structure of sulfonated-eumelanin can withstand the photolithography process allowing patterning down to a micrometer scale. This approach opens the possibility of integrating synthetic sulfonated-eumelanin thin-films into robust solid-state platforms to create novel bio(inspired) devices [30–33] without using unconventional methodologies like Parylene-C or silk fibroin. Finally, the patterned sulfonated-eumelanin film exhibited a straightforward two-electrode system's pH and humidity sensing potential.

2. Experimental section

2.1. Sulfonated-eumelanin synthesis

Sulfonated-eumelanin (SMel) was synthesized following Ref. [34]. Briefly, in a round bottom flask with 200 mL of dimethylsulfoxide (DMSO, Vetec) under stirring, a mixture of 1.50 g of 3, 4–dihydroxy-DL-phenyl-alanine (Sigma-Aldrich) and 0.93 g of benzoyl peroxide (*Êxodo Química*) were dissolved. The solution was maintained in reflux in an oil bath (100 °C) for 13 days. Then, the flask was opened, and the temperature increased to 140 °C to reduce the solution volume to ~50 mL. Next, the concentrated mixture was cooled to room temperature, dissolved in 150 mL of acetonitrile (Synth), and centrifuged (2500 rpm for 15 min) after 24 h. Finally, the precipitate was recovered and dried in the oven (90 °C).

2.2. SMel thin-film deposition

For the SMel film deposition, glass substrates were cleaned using a three-step procedure: (i) 30 min/each ultrasonic bath in acetone PA, acetone VLSI, isopropanol alcohol VLSI, and dried with nitrogen; (ii) piranha solution (H_2SO_4/H_2O_2, 2:1 in volume) at 100 °C for 10 min, and; (iii) 5 min in O_2 plasma.

SMel films were deposited through two-step spin-coating (500 rpm for 5 s and 2000 rpm for 60 s) using a 30 mg.mL^{-1} solution in DMSO (D350, Techni Strip® Micro, France). After the deposition, the film was heated at 100 °C for two min, and this procedure was repeated three

times. The final SMel layer was stored in a desiccator.

2.3. Fabrication of SMel micropatterned

The SMel thin-film patterning was obtained using conventional photolithography. Initially, the SMel was covered with an AZ 5214E photoresist (Microchemicals) layer through two-step spin-coating (40 s at 3000 rpm and 5 s at 5000 rpm), followed by baking at 120 °C for 5 min. Then, the heterostructure was transferred to a direct prototyping ML3 (DMO) mask aligner (wavelength 5 nm). The desired pattern was exposed to UV light (110 mJ.cm^{-2} in the wavelength range of 385–405 nm), and the crosslinked area was removed by immersing the film in AZ 726 MIF developer (Merk, Germany). Next, the SMel unprotected film passes through a soft bake at 100 °C for 5 min, and it is then etched by oxygen-reactive ion etching (O_2-RIE). Finally, the remaining photoresist was removed by immersing the samples in a heated acetone VLSI for 2 min under gentle mechanical agitation.

2.4. Morphological & structural characterizations

A Park NX10 atomic force microscopy (AFM) was used to obtain topography images, and they were processed and treated with Gwyddion software (v. 2.59). LSCM VK-X200 (Keyence), with a wavelength of 408 nm, was used for confocal laser scanning microscopy images.

Thermogravimetry analysis of SMel powder was obtained using a STA 449F3 Netzsch thermogravimetric analyzer in the range of 27–700 °C under atmospheric air at a heating rate of 10 °C.min^{-1}. The Raman spectra were acquired using a Confocal Raman XploRa™ Plus (HORIBA) spectrometer equipped with a CCD detector and an optical microscope Olympus BX. It was operated with high-resolution grating (1800 grooves.mm^{-1}), 50 × lens, laser excitation at 532 nm with 10% of maximum power, 30 s exposure time, and five accumulations in the static mode under atmospheric conditions.

X-ray photoelectron spectroscopy (XPS) measurements were obtained on a Thermo Scientific K-alpha (Thermo Scientific, Inc.) spectrometer with less than 10^{-7} Pa pressure. A monochromatic AlKα X-ray (1486.7 eV) source was focused in a region with a 300 μm diameter. Survey scans were collected with a pass energy of 200 eV, 1.0 eV step size, and fifth sweeps at 10 s dwell time for electron counting to improve the signal/noise ratio. In addition, high-resolution spectra were obtained with a pass energy of 50 eV, 0.1 eV step size, with ten sweeps at 50 s dwell time. A Shirley background with mixed Gaussian-Lorentzian peaks (with 30% Lorentzian character) was used to fit the raw data in CasaXPS.

2.5. Device fabrication & electrical characterization

Twelve interdigitated metal electrodes (IDE) were patterned on a 25×25 mm clean glass (see the three-step procedure of Section 2.2). Conventional photolithography with AZ 5214E photoresist followed by e-beam evaporation of chromium/gold (Cr/Au, 20/20 nm) was used. Both metallic layers were deposited at 0.6 Å.s^{-1} under 0.13 mPa. As a result, each IDE has a 4 mm^2 active area with a 20 μm distance between electrode arrays (channel length), resulting in a width-length (W/L) ratio of 4240. Later, SMel films and patterns (12 nm thickness) were obtained following the procedures described in Section 2.2. A schematic of the final devices is shown in Fig. S1 in the Supplementary Material.

The current *vs.* voltage (I-V) characteristics were taken in dual sweep mode using a step voltage fixed at 20 mV in the range from −1 V to 1 V DC. Transient measurements were carried at a fixed current of 100 nA or a fixed voltage of 100 mV. A probe station equipped with an optical microscope and tungsten tips connected to micromanipulators using a Keithley Semiconductor Parameter Analyzer 4200-SCS, which has a limit of 10^{-15} A, was used for DC and transient measurements. AC measurements were recorded with an impedance analyzer Solartron model SI 1260A in the frequency range of 10^{-1} to 10^6 Hz, swept from

high to low frequencies, with sine-wave voltage signal amplitude of 100 mV and 0 V offset DC bias.

Three different relative humidity (RH) levels were used for the humidity sensors: N$_2$, 60%, and 100%. N$_2$ atmosphere ($\sim$ 6% RH) was achieved by placing the IDEs inside a homemade chamber with a flow of N$_2$ gas for at least one hour; 60 ($\pm$ 10)% at room atmosphere and 100% in contact with deionized water. In the case of the pH sensor, 0.1 M of sodium phosphate monobasic (NaH$_2$PO$_4$, Sigma-Aldrich) and sodium phosphate dibasic (Na$_2$HPO$_4$, Sigma-Aldrich) PBS buffer solution was used. Sodium hydroxide (NaOH, Merck) and nitric acid (HNO$_3$, Synth) were added to the PBS solution to obtain pH ranging from 8 to 5.

3. Results and discussion

3.1. Micropatterning of SMel thin-film

Our focus is on enhancing the integration capability of SMel for a broad range of technological applications. Hence, the SMel micropatterns on glass substrates were fabricated via a standard photolithography process (Fig. 2(a)). First, the AZ 5214E (as a positive) photoresist was cast on the SMel film, and then UV light was exposed through a photolithographic mask to transfer the structure pattern. After developing the crosslinked photoresist, a soft backing was followed by removing the unprotected SMel by O$_2$-RIE. High-fidelity patterned structures down to 200–300 μm of lateral dimension are shown in Fig. 2 (b). Thermogravimetry analysis of SMel powder (Fig. S2 and detailed discussion in the Supplementary material) indicates that during backing (at 100 and 120 °C), only desorption of water and DMSO is expected [39]. Therefore, we do not expect that the SMel film is affected at this temperature range.

We compare the surface topography by AFM images and the chemical composition by Raman spectroscopy and XPS of SMel films before (pristine) and after (patterned) the photolithographic patterning. The AFM images show no topographic changes, including excellent uniformity and the absence of defects (pinholes and agglomerates), in a 5 μm x 5 μm scanned area, Fig. 3(a). The homogeneous surface roughness, estimated via root-mean-square (RMS), was found below 1 nm for both cases. Raman spectra (Fig. 3(b)) exhibit the dominant modes of band D (1335 cm^{-1}) and G (1579 cm^{-1}) from vibrational modes of disordered graphitic-like carbon [35], which indicates that SMel's carbon organization is not affected by the photolithography process. Further analysis with XPS also confirms no significant changes. As demonstrated in Fig. 3 (c) by the XPS survey scan with associated analysis (Fig. 3(d and e) and discussion of the high-resolution spectra in Fig. S3-S4 and Table S1), the chemical composition of both films is compatible with SMel [36]. Nonetheless, the patterned film shows a slight decrease in the S2p intensity (about 30%, especially in the region between 166 and 170 eV) compared to pristine. This behavior is most likely related to the instability of the sulfonated groups [27,37]. Still, it is necessary to stress that the atomic composition of carbon, oxygen, and nitrogen are not affected, indicating that the basic SMel indole structure does not lose its integrity.

Therefore, our results demonstrate that the indole structure of eumelanin-based materials can withstand a standard photolithography process without substantial changes, which could compromise the film integration. The scalability of this technique, towards micropatterned topology, allows large-scale production of eumelanin-based microscale devices or macroscale objects with several eumelanin-based microdevices interconnected.
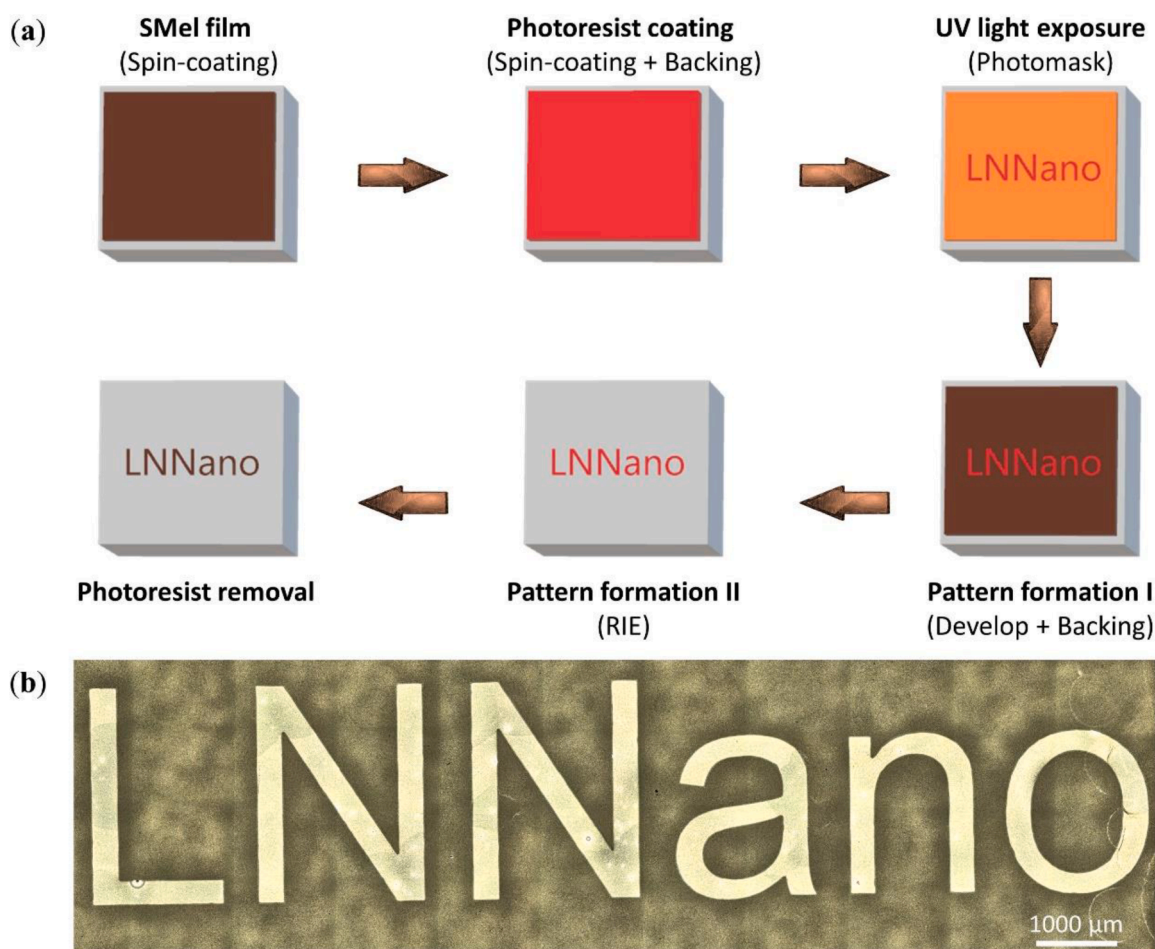

Fig. 2. (a) Schematic fabrication process to generate SMel patterns and (b) its optical image.
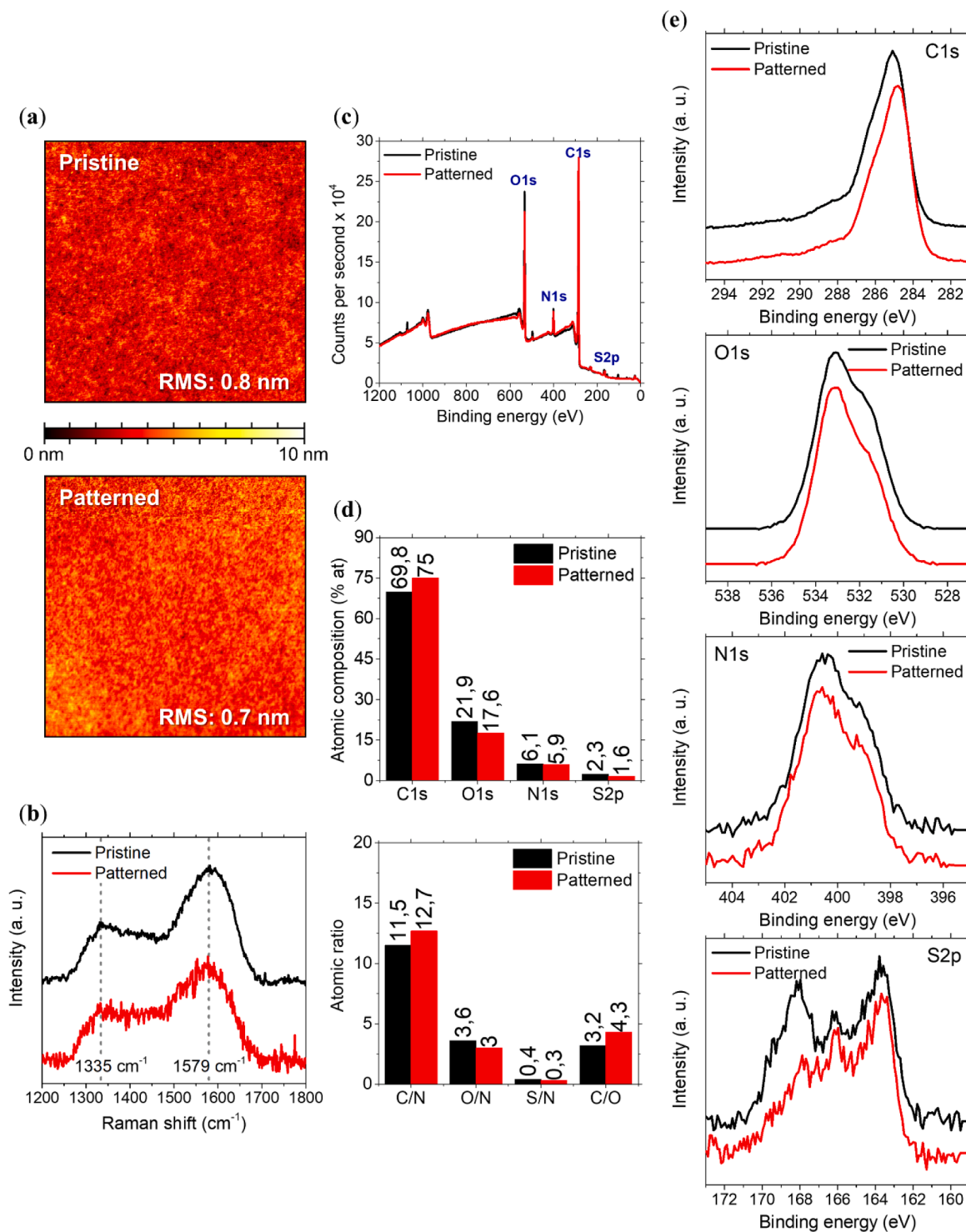
(a)

(c)

(e)

(d)

(b)

Fig. 3. (a) 5 μm x 5 μm AFM topography image of the pristine (top) and patterned (bottom) SMel films on glass. (b) Raman spectra and (c) XPS survey scan for SMel films before and after the photolithography process. (d) Chemical composition (atomic%), atomic ratios, and (e) C1s, N1s, O1s, and S2p high-resolution XPS spectra of pristine and patterned SMel films. Spectra simulations and functional group intensities are shown in Supplementary material (Figs. S3 and S4 and Table S1).

3.2. Electrical behavior of SMel patterned thin-film

One of the eumelanin's most critical properties is its hydration-dependent conductivity and solid-state protonic conductivity [10,11]. Hence, we have patterned SMel thin-films on a gold IDE (Fig. S1a) to evaluate if the photolithography process affects its charge transport behavior and determine their electrical response to different humidity levels: N_2, 60%, and 100%. For comparison, the pristine SMel films were

also analyzed using the same IDE geometry. As shown in Fig. 4(a, b), SMel films exhibit an excellent response to changes in the relative humidity (RH), with the conductivity (Fig. 4(c, d)) increasing more than five orders of magnitude as RH rise from N_2 to 100%. The most notable difference was a conductivity variation of 70% when we compared both systems at 60% RH. This result is associated with RH variation in the room atmosphere during the measurements on dry and wet days ($\sim$ 50% and $\sim$ 70% RH, respectively, obtained with a commercial humidity
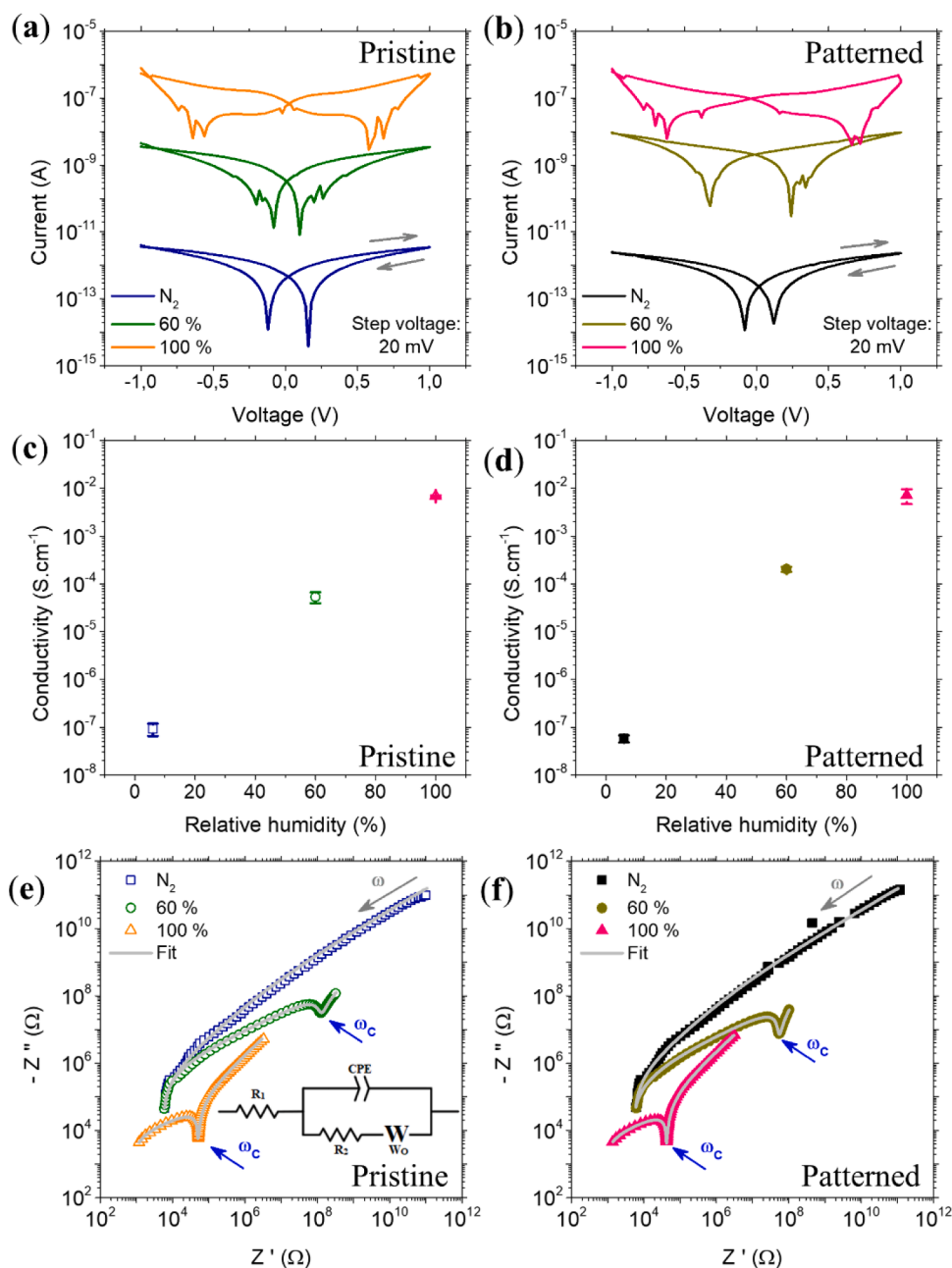
Fig. 4. Electrical behavior of pristine (left) and patterned (right) SMel films over the different RHs. (a, b) The log-linear plot of the current *vs.* voltage response. Eight different devices in a group of four substrates were measured. (c, d) SMel's conductivity normalized by the system geometry and film thickness. (e, f) EIS response on a log-log plot. Symbols represent the experimental data, whereas straight-line fit using the Randles minimalist equivalent circuit (inset in Fig. 4(e)). The same data set is shown in Fig. S5 on a linear scale. Fitting parameters are shown in Table S2. The characteristic frequency ω_c is indicated by the blue arrow.

sensor).

To further assess the electrical behavior under the different RHs, we show the humidity-dependent Nyquist plots on a log-log scale in Fig. 4 (e, f). The same data set is displayed on a linear scale in Fig. S5. The data shows a semicircle-like dependence in the low impedance region (higher frequency), coupled with a line or Warburg tail at higher impedance (low frequency) assigned to diffusion-limited processes. The exception is N_2 RH which does not show the tail feature. These regimes are separated at a frequency ω_c, shown by the blue arrow, and are compatible with the expected eumelanin-based materials [7–9]. The EIS can be analyzed using the Randles electrical equivalent circuit, inset in Fig. 4(e). The Randles circuit considers the contact resistance given by a resistor R_1, the surface modification capacitance and dielectric double-layer by a constant phase element CPE, ionic dissipation current with a second resistor R_2, and the mass diffusion at the blocking electrode interface by a Warburg open-element [8,9]. The fitting parameters are reported in Table S2.

As shown in Fig. 4(e, f), the decrease in RH is accompanied by an increase in the semicircle and a reduction in the tail at the high-impedance region of the plot. Such observation is an unmistakable signature of non-functionalized and sulfonated eumelanin ionic conductivity driven by the water-induced comproportionation equilibrium reaction [8,9]. This equilibrium proposes that protons (in the form of H_3O^+) and semiquinones (SQ) will be originated in the presence of water after the interaction of fully oxidized (IQ) and fully reduced (HQ) monomeric units (IQ + HQ + $2H_2O \rightleftarrows 2H_3O^+ + 2SQ$). Hence, the amount of charge carrier will decrease upon decreasing the water content, leading to lower conductivity. Notice that the presence of the sulfonated moieties in the SMel structure (Fig. 1(b)) does not hinder the existence of the comproportionation equilibrium, as previously demonstrated by electrical and electron paramagnetic resonance measurements [9,38,39]. Therefore, based on the similarities between our results and the literature [9,39], we can affirm that the pattern process does not alter the charge transport behavior of SMel.

3.3. Sensing performance

To validate the applicability of the SMel patterned films, we have explored them in a series of sensing applications. As a sensory platform, we explore standard interdigitate electrodes (Fig. S1), a simple structure well studied in the sensing literature [40–52].

The standard sulfonated-eumelanin (which has a synthesis time of 60 days compared to the 13 days of SMel) is a promising candidate for a pH sensorial platform [16,53]. Hence, the pH sensibility of our patterned films was investigated by applying a small current between the two electrodes to measure a voltage across the patterned films over time (Fig. S6(a)). Four different pHs values were chosen around the physiological condition (pH 5, pH 6, pH 7, and pH 8), the best performance range of the standard sulfonated-eumelanin [16]. The voltage drop decreases stepwise as the pH is varied upon controlled pH solutions. The response of the SMel patterned film to pH, Fig. 5(a), shows a clear linear trend in the voltage to pH within the range of acidic (pH 5) to basic (pH

8). The linear V/pH correlation allowed us to obtain a sensitivity of 50.1 mV.pH^{-1} with outstanding reproducibility. To further evaluate the long-term reproducibility of the device, we measured the pH response at pH 5 and then at pH 8, repeating this cycle five times. As a result, we observe a reduction of *c.a.* 6% of the pH sensibility after the 5th cycle (Fig. S6(b)). This decrease indicates that the device is sensitive, robust, and stable for prolonged applications. Interestingly, our two-terminal device showed a similar sensibility to other eumelanin-based pH sensors, as previously demonstrated for an extended-gate field-effect transistor (48.9 mV.pH^{-1}, in the pH range of 2–12, 0.1 M phosphate/citrate buffer solution) [15] and electrochemical sensor (62 mV.pH^{-1}, in the pH range of 5–8, 5 mM potassium ferricyanide/potassium ferrocyanide buffer solution) [16,53]. The differences could be related to the device's geometries (three *vs.* two terminals) and different experimental conditions (pH range or buffer solutions). Also, these studies evaluated different NF-eumelanin or standard sulfonated-eumelanin, which implies that each sample has particular structural (for instance,
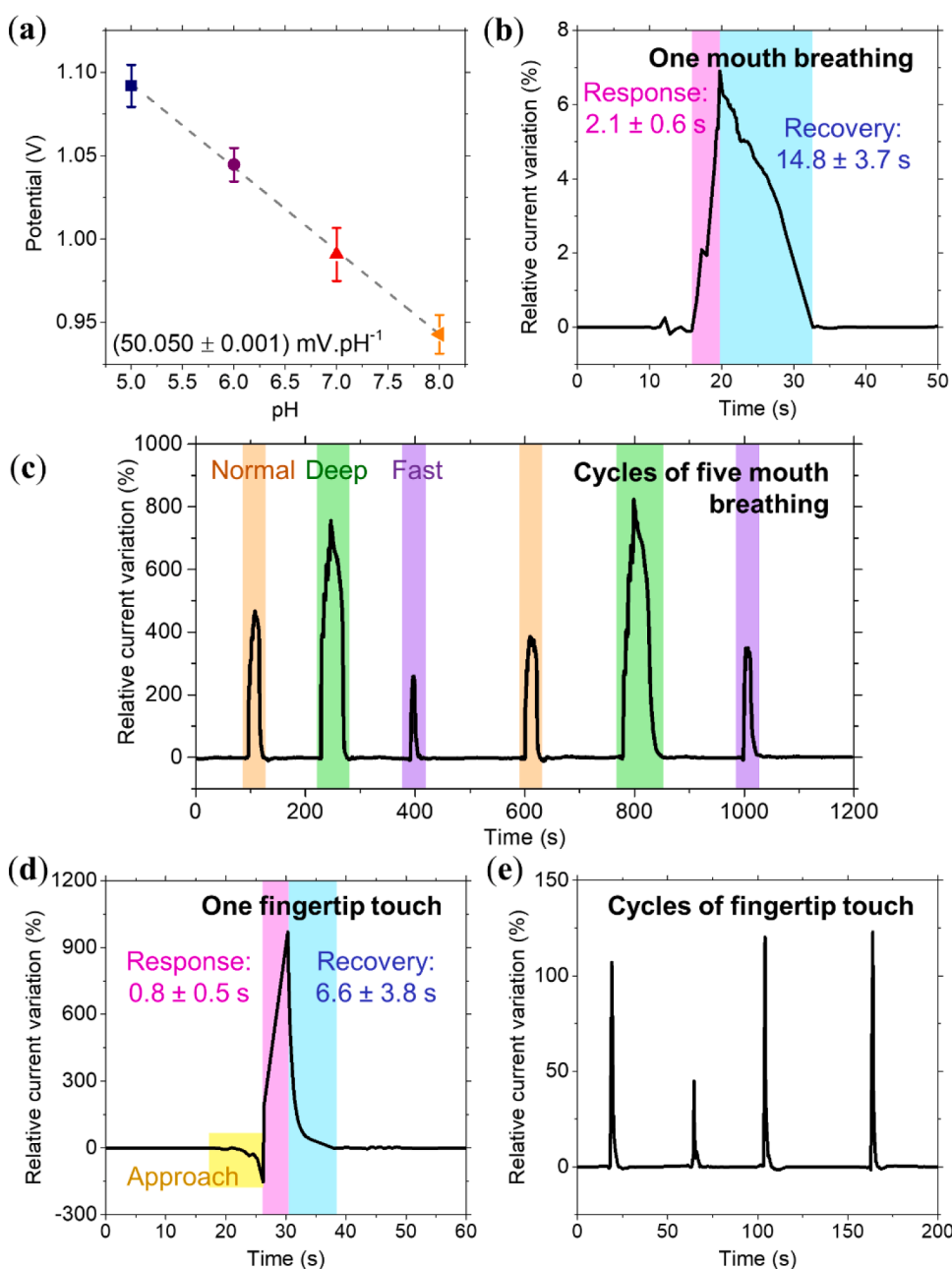

Fig. 5. (a) pH sensor performance under physiological conditions. Each data is a standard deviation of five different devices. (b) Response and recovery times of humidity sensor in response to one human mouth-breathing stimuli at a normal rate. (c) The cycling behavior of the humidity sensor for five mouth-breathing at normal, deep, and fast rates. (d) Response and recovery times of pressure sensor in response to human fingertip touch stimuli. (e) The cycling behavior of the pressure sensor under external stimuli from human fingertip touch.

DHI/DHICA ratio) and morphological features resulting in specific interactions with the electrolyte.

To analyze the sensing performance of the patterned SMel film in a real everyday life external stimulus, we have explored the dynamic response to human exhaled breath (humidity sensor) and human fingertip touch (contact sensor). In Fig. 5(b), one typical human mouth-breathing humidity test is shown by the relative current variation (the ratio between the change in current and the initial current). When the SMel film was exposed to the moisture of the mouth breathing, the current quickly increased, reaching its maximum value within 2.1 ± 0.6 s (response time). Once the breath ended, the current instantly decreased, taking 14.8 ± 3.7 s to return to its initial value (recovery time). Both fast response and longer recovery time are explained considering eumelanin's porous and hydrophilic nature, making water desorption challenging [54]. An ultrafast humidity sensor (~ 0.45 s and ~ 0.45 response and recovery times, respectively) based on dopamine-melanin has been reported in the literature [42]. The difference in time response between both systems can be related to film thickness and potentially the final RH equilibrium value [55], as we are using breathing as a source of moisture. Compared to other natural and synthetic materials applied to the same application, our time response is at the fastest range while keeping the recovery the same [43,44,46,51]. For a comparison between our device parameters to other natural and inorganic materials (in a series of humidity applications), see Table S3.

The SMel humidity sensor presented here showed good dynamic responses to repeated mouth-breathing when no external stimuli were applied between breathing (Fig. S6(c)). Hence, we evaluate five cycles of mouth-breathing at three different rates: normal, deep, and fast. Fig. 5 (c) indicates that it is challenging to distinguish the sensor's response to different breathing rates because we cannot identify all five stimuli, unlike other rapid-response wearable humidity sensors [43,44,46,56]. This effect is most likely related to eumelanin's porous and hydrophilic nature that hinders the complete water desorption between breaths and is in line with the increase of relative current variation based on its humidity-dependent electrical behavior (Section 3.2). Nonetheless, it is possible to see that the overall signal width changes for the different rates (18.8 ± 3.7 s for normal, 42.0 ± 7.6 s for deep, and 10.1 ± 3.0 s for fast rates). This effect could be used to distinguish breathing patterns in future studies.

We also evaluated the sensor's response to human touch, and the results are shown in Fig. 5(d). The contact sensor reaches its maximum current within 0.8 ± 0.5 s, with a recovery time of 6.6 ± 3.8 s and excellent repeatability (Fig. 5(e)). Additionally, our contact response displays a current decrease in an exponential behavior before the sensing signal, Fig. 5(d), which can be understood as the sensor's sensibility to the fingertip approaching along the z-direction [43]. Several possibilities can explain the sensing capability: pressure, temperature, skins' moisture, and electrostatic proximity sensing [43]. In a simple attempt to shed some light on this system, we have repeated the same experiment but using nitrile gloves. It was impossible to distinguish the sensor signal and the baseline noise (Fig. S6(d)). Consequently, one can assume that the moisture from the skin plays a significant role in contact sensing and is responsible for the change in the relative variation current between Fig. 5(d) and Fig. 5(e). The high recovery time observed, compared to the literature (usually in milliseconds) [43,57–60], could also be explained by considering the skin moisture because it would increase the number of water molecules significantly in the system. A more considerable time would be necessary to desorb most of them. We also should mention that all the different device structures and methodologies employed (such as capacitance over time and periodic resonant frequency) could also be responsible for the differences in response and recovery times. It is worth pointing out that a deeper analysis of the human breath and touch sensing response is beyond the scope of this work. However, as there has been no report on eumelanin-based respiratory and pressure-sensing capabilities in the literature, our results indicate that it can be a promising material for these applications.

Detailed analysis with a more robust device structure and precise hydration control should improve sensing performance. Also, as SMel is known to have a weaker interaction with water [9,11,38], optimizing the film characteristics could also boost the device's performance.

Given the above results, we indicate some potential directions for the sensing technology using eumelanin and eumelanin-based materials. The humidity is a parameter of extreme importance nowadays with the rapid advancement of wearable electronic devices for non-contact detecting respiratory behavior [41,50,56] and skin moisture recognition [61], as well as one of the critical physiological signs for personal healthcare [62]. Based on the significant improvement of the conductivity with water content, Fig. 3(b), and the sensing characteristic, Fig. 5 (b-d), SMel is a great biocompatible candidate to sense changes in the human body moisture. Additionally, the touch sensing capability allied with body moisture (Fig. 5(d)) could sustain direction, force, motion, and proximity multifunctionalities for an electronic skin [63–65]. Combining the biodegradability of sulfonated compounds [66–68] with the one from NF-eumelanin structure [2] can also make SMel a material for wearable and potential transient electronic devices for health monitoring [65,69,70].

In our forecast for wearable electronic devices, SMel pH sensing is a promising candidate for real-time wound healing management. Indeed, it is known that slightly acidic pH can provide the wound with optimum healing conditions. In contrast, pH ranging from 7 to 8 are hard-to-heal injuries with the potential presence of bacterial infections [71–74]. Hence, developing smart bandages with biocompatible and eco-friendly materials is possible. Using eumelanin, for instance, one can develop a real-time, noninvasive bandage capable of monitoring wound healing precisely. It may also reduce healthcare costs since chronic wounds are highly costly and are acknowledged as a significant source of mortality for diabetic and bed-ridden patients [71–74]. This proposition is further reinforced considering that standard sulfonated-eumelanin did not lose its pH sensibility in human blood plasma [16] and bacteria cultural media [53].

To conclude, it should be emphasized that the consolidated technology of pH sensing already spread through the consumer market is challenging to be adapted to wound monitoring due to safety and conformability regulations. Although we have used a glass substrate as a proof-of-concept, we believe that the pH sensor used in this study could be extended towards flexible substrates like paper [41,75] and textile [74] to bring more comfort to the patient. Natural rubber latex is also a promising flexible substrate for a noninvasive smart bandage. One additional advantage is that the wound healing process would be accelerated by the presence of both latex [76] and eumelanin [77,78].

4. Conclusion

We demonstrate that the basic indole structure of a eumelanin-based material can withstand the standard photolithography process, delivering a high-fidelity pattern down to microscale without changing its primary structure and charge-transport behavior. To test the applicability of the SMel patterned films, a multisensory platform based on a simple two-terminal device was used for pH and humidity sensing. Our pH sensor demonstrates the efficiency of 50.1 mV.pH^{-1} within the physiologically pH levels (between pH 5 and pH 8) and stability over time. These features are well suited for wound healing monitoring. Furthermore, the humidity sensor shows excellent conductivity, switching about five orders of magnitude from dry to wet conditions. In addition, good response and recovery times from human breath are evidenced. The approach presented here represents a step toward miniaturized wearable technologies that integrate eumelanin materials connected to portable circuitry for human healthcare and physiological monitoring.

Data availability

Data supporting the findings of this study are available from the corresponding authors upon reasonable request.

CRediT authorship contribution statement

João V. Paulin: Conceptualization, Methodology, Validation, Formal analysis, Investigation, Writing – original draft, Writing – review & editing, Visualization. **Luiz G.S. Albano:** Methodology, Resources, Writing – review & editing. **Davi H.S. Camargo:** Investigation, Writing – review & editing. **Mariane P. Pereira:** Investigation, Resources, Writing – review & editing. **Bruna A. Bregadiolli:** Investigation, Resources, Writing – review & editing. **Carlos F.O. Graeff:** Resources, Writing – review & editing. **Carlos C.B. Bufon:** Writing – review & editing, Supervision, Project administration, Funding acquisition.

Declaration of Competing Interest

The authors declare that they have no known competing financial interests or personal relationships that could have appeared to influence the work reported in this paper.

Acknowledgments

Supplementary materials

Supplementary material associated with this article can be found, in the online version, at doi:10.1016/j.apmt.2022.101525.

References

[1] P. Meredith, T. Sarna, The physical and chemical properties of eumelanin, Pigment Cell Res. 19 (2006) 572–594, https://doi.org/10.1111/j.1600-0749.2006.00345.x.

[2] E. Di Mauro, D. Rho, C. Santato, Biodegradation of bio-sourced and synthetic organic electronic materials towards green organic electronics, Nat. Commun. 12 (2021) 3167, https://doi.org/10.1038/s41467-021-23227-4.

[3] M.R. Powell, B. Rosenberg, The nature of the charge carriers in solvated biomacromolecules, Bioenergetics 1 (1970) 493–509, https://doi.org/10.1007/BF01517187.

[4] M.M. Jastrzebska, H. Isotalo, J. Paloheimo, H. Stubb, Electrical conductivity of synthetic DOPA-melanin polymer for different hydration states and temperatures, J. Biomater. Sci. Polym. Ed. 7 (1995) 577–586, https://doi.org/10.1163/156856295x00490.

[5] N. Amdursky, E.D. Głowacki, P. Meredith, Macroscale biomolecular electronics and ionics, Adv. Mater. 31 (2019) 1802221. 10.1002/adma.201802221.

[6] A.B. Mostert, B.J. Powell, F.L. Pratt, G.R. Hanson, T. Sarna, I.R. Gentle, P. Meredith, Role of semiconductivity and ion transport in the electrical conduction of melanin, Proc. Natl. Acad. Sci. USA. 109 (2012) 8943–8947, https://doi.org/10.1073/pnas.1119948109.

[7] J. Wünsche, Y. Deng, P. Kumar, E. Di Mauro, E. Josberger, J. Sayago, A. Pezzella, F. Soavi, F. Cicoira, M. Rolandi, C. Santato, Protonic and electronic transport in hydrated thin films of the pigment eumelanin, Chem. Mater. 27 (2015) 436–442, https://doi.org/10.1021/cm502939r.

[8] M. Sheliakina, A.B. Mostert, P. Meredith, Decoupling ionic and electronic currents in melanin, Adv. Funct. Mater. 28 (2018), 1805514, https://doi.org/10.1002/adfm.201805514.

[9] J.V. Paulin, A.P. Coleone, A. Batagin-Neto, G. Burwell, P. Meredith, C.F.O. Graeff, A.B. Mostert, Melanin thin-films: a perspective on optical and electrical properties, J. Mater. Chem. C 9 (2021) 8345–8358, https://doi.org/10.1039/D1TC01440D.

[10] A.B. Mostert, Melanin, the what, the why and the how: an introductory review for materials scientists interested in flexible and versatile polymers, Polymers 13 (2021) 1670, https://doi.org/10.3390/polym13101670 (Basel).

[11] J.V. Paulin, C.F.O. Graeff, From nature to organic (bio)electronics: a review on a melanin-inspired material, J. Mater. Chem. C 9 (2021) 14514–14531, https://doi.org/10.1039/D1TC03029A.

[12] Y.J. Kim, W. Wu, S. Chun, J.F. Whitacre, C.J. Bettinger, Biologically derived melanin electrodes in aqueous sodium-ion energy storage devices, Proc. Natl. Acad. Sci. 110 (2013) 20912–20917. 10.1073/pnas.1314345110.

[13] Y.J. o. Kim, W. Wu, S.E. Chun, J.F. Whitacre, C.J. Bettinger, Catechol-mediated reversible binding of multivalent cations in eumelanin half-cells, Adv. Mater. 26 (2014) 6572–6579, https://doi.org/10.1002/adma.201402295.

[14] M. Sheliakina, A.B. Mostert, P. Meredith, An all-solid-state biocompatible ion-to-electron transducer for bioelectronics, Mater. Horizons. 5 (2018) 256–263, https://doi.org/10.1039/C7MH00831G.

[15] M. Piacenti-Silva, J.C. Fernandes, N.B. de Figueiredo, M. Congiu, M. Mulato, C.F. de O. Graeff, Melanin as an active layer in biosensors, AIP Adv. 4 (2014), 037120, https://doi.org/10.1063/1.4869638.

[16] Z. Tehrani, S.P. Whelan, B. Mostert, J.V. Paulin, M.M. Ali, E.D. Ahmadi, C.F. de O. Graeff, O.J. Guy, D.T. Gethin, Printable and flexible graphene pH sensors utilising Thin film melanin for physiological applications, 2D Mater. 7 (2020), 024008, https://doi.org/10.1088/2053-1583/ab72d5.

[17] P. Kumar, E. Di Mauro, S. Zhang, A. Pezzella, F. Soavi, C. Santato, F. Cicoira, Melanin-based flexible supercapacitors, J. Mater. Chem. C 4 (2016) 9516–9525, https://doi.org/10.1039/c6tc03739a.

[18] J.V. Paulin, S.L. Fernandes, C.F.O. Graeff, Solid-state electrochemical energy storage based on soluble melanin, Electrochem 2 (2021) 264–273, https://doi.org/10.3390/electrochem2020019.

[19] L.G.S. Albano, J.V. Paulin, L.D. Trino, S.L. Fernandes, C.F. de O. Graeff, Ultraviolet-protective thin film based on PVA–melanin/rod-coated silver nanowires and its application as a transparent capacitor, J. Appl. Polym. Sci. 136 (2019) 47805, https://doi.org/10.1002/app.47805.

[20] V. Ball, I. Nguyen, M. Haupt, C. Oehr, C. Arnoult, V. Toniazzo, D. Ruch, The reduction of Ag+ in metallic silver on pseudomelanin films allows for antibacterial activity but does not imply unpaired electrons, J. Colloid Interface Sci. 364 (2011) 359–365, https://doi.org/10.1016/j.jcis.2011.08.038.

[21] M. Araújo, R. Viveiros, A. Philippart, M. Miola, S. Doumett, G. Baldi, J. Perez, A.R. Boccaccini, A. Aguiar-Ricardo, E. Verné, Bioactivity, mechanical properties and drug delivery ability of bioactive glass-ceramic scaffolds coated with a natural-derived polymer, Mater. Sci. Eng. C 77 (2017) 342–351, https://doi.org/10.1016/j.msec.2017.03.169.

[22] E. Di Mauro, R. Xu, G. Soliveri, C. Santato, Natural melanin pigments and their interfaces with metal ions and oxides: emerging concepts and technologies, MRS Commun. 7 (2017) 141–151, https://doi.org/10.1557/mrc.2017.33.

[23] J. Wang, H. Liu, Y. Liu, C. Chu, Y. Yang, Y. Zeng, W. Zhang, G. Liu, Eumelanin-Fe3O4 hybrid nanoparticles for enhanced MR/PA imaging-assisted local photothermolysis, Biomater. Sci. 6 (2018) 586–595, https://doi.org/10.1039/c8bm00003d.

[24] A.B. Mostert, S. Rienecker, M. Sheliakina, P. Zierep, G.R. Hanson, J.R. Harmer, G. Schenk, P. Meredith, Engineering proton conductivity in melanin using metal doping, J. Mater. Chem. B 8 (2020) 8050–8060, https://doi.org/10.1039/D0TB01390K.

[25] Y.H. Youn, S. Pradhan, L.P. Da Silva, I.K. Kwon, S.C. Kundu, R.L. Reis, V.K. Yadavalli, V.M. Correlo, Micropatterned silk-fibroin/eumelanin composite films for bioelectronic applications, ACS Biomater. Sci. Eng. 7 (2021) 2466–2474, https://doi.org/10.1021/acsbiomaterials.1c00216.

[26] C. Yumusak, N.S. Sariciftci, M. Irimia-Vladu, Purity of organic semiconductors as a key factor for the performance of organic electronic devices, Mater. Chem. Front. 4 (2020) 3678–3689, https://doi.org/10.1039/d0qm00690d.

[27] J.P.B. Cuba, G.G.B. Alves, L.A. Galindo, J.V. Paulin, A. Batagin-Neto, Sulfonated melanin derivatives: theoretical evaluation of local reactivities and chemical structures, J. Mol. Model. 27 (2021) 362, https://doi.org/10.1007/s00894-021-04982-z.

[28] M. Piacenti-Silva, A.A. Matos, J.V. Paulin, R.A. da S. Alavarce, R.C. de Oliveira, C.F. Graeff, Biocompatibility investigations of synthetic melanin and melanin analogue for application in bioelectronics, Polym. Int. 65 (2016) 1347–1354, https://doi.org/10.1002/pi.5192.

[29] J.V. Paulin, A.G. Veiga, Y. Garcia-Basabe, M.L.M. Rocco, C.F. Graeff, Structural and optical properties of soluble melanin analogues with enhanced photoluminescence quantum efficiency, Polym. Int. 67 (2018) 550–556, https://doi.org/10.1002/pi.5543.

[30] K. Torikai, R. Furlan de Oliveira, D.H. Starnini de Camargo, C.C. Bof Bufon, Low-voltage, flexible, and self-encapsulated ultracompact organic thin-film transistors based on nanomembranes, Nano Lett. 18 (2018) 5552–5561, https://doi.org/10.1021/acs.nanolett.8b01958.

[31] L.G.S. Albano, T.P. Vello, D.H.S. De Camargo, R.M.L. Da Silva, A.C.M. Padilha, A. Fazzio, C.C.B. Bufon, Ambipolar resistive switching in an ultrathin surface-supported metal-organic framework vertical heterojunction, Nano Lett. 20 (2020) 1080–1088, https://doi.org/10.1021/acs.nanolett.9b04355.

[32] A. Nawaz, L. Merces, D.M. de Andrade, D.H.S. de Camargo, C.C. Bof Bufon, Edge-driven nanomembrane-based vertical organic transistors showing a multi-sensing capability, Nat. Commun. 11 (2020) 841, https://doi.org/10.1038/s41467-020-14661-x.

[33] L.M.M. Ferro, L. Merces, D.H.S. de Camargo, C.C. Bof Bufon, Ultrahigh-gain organic electrochemical transistor chemosensors based on self-curled nanomembranes, Adv. Mater. 33 (2021), 2101518, https://doi.org/10.1002/ADMA.202101518.

[34] M. Piacenti-Silva, E.S. Bronze-Uhle, J.V. Paulin, C.F.O. Graeff, Temperature-enhanced synthesis of DMSO-Melanin, J. Mol. Struct. 1056–1057 (2014) 135–140, https://doi.org/10.1016/j.molstruc.2013.10.041.

[35] L.G.S. Albano, E. Di Mauro, P. Kumar, F. Cicoira, C.F.O. Graeff, C. Santato, Novel insights on the physicochemical properties of eumelanins and their DMSO derivatives, Polym. Int. 65 (2016) 1315–1322, https://doi.org/10.1002/pi.5167.

[36] J.V. Paulin, J.D. Mcgettrick, C.F.O. Graeff, A.B. Mostert, Melanin system composition analyzed by XPS depth profiling, Surf. Interface 24 (2021), 101053, https://doi.org/10.1016/j.surfin.2021.101053.

[37] E.S. Bronze-Uhle, A. Batagin-Neto, P.H.P. Xavier, N.I. Fernandes, C.F.O. Graeff, Synthesis and characterization of melanin in DMSO, J. Mol. Struct. 1047 (2013) 102–108, https://doi.org/10.1016/j.molstruc.2013.04.061.

[38] J.V. Paulin, A. Batagin-Neto, P. Meredith, C.F.O. Graeff, A.B. Mostert, Shedding light on the free radical nature of sulfonated melanins, J. Phys. Chem. B 124 (2020) 10365–10373, https://doi.org/10.1021/acs.jpcb.0c08097.

[39] B.A. Bregadiolli, J.V. Paulin, L.G.S. Albano, L.M. Martins, D.H.S. de Camargo, L.C. da S. Filho, C.C.B. Bufon, C.F. de O. Graeff, A strategy towards melanin-based functional material: rGO and sulfonated melanin composites, J. Mater. Chem. C 9 (2021) 16991–17002, https://doi.org/10.1039/D1TC02749B.

[40] D. Zhang, J. Tong, B. Xia, Humidity-sensing properties of chemically reduced graphene oxide/polymer nanocomposite film sensor based on layer-by-layer nano self-assembly, Sensors Actuat. B Chem. 197 (2014) 66–72, https://doi.org/10.1016/j.snb.2014.02.078.

[41] F. Güder, A. Ainla, J. Redston, B. Mosadegh, A. Glavan, T.J. Martin, G.M. Whitesides, Paper-based electrical respiration sensor, Angew. Chemie Int. Ed. 55 (2016) 5727–5732, https://doi.org/10.1002/anie.201511805.

[42] T.F. Wu, J.D. Hong, Synthesis of water-soluble dopamine–melanin for ultrasensitive and ultrafast humidity sensor, Sensors Actuat. B Chem. 224 (2016) 178–184.

[43] J.M. Nassar, M.D. Cordero, A.T. Kutbee, M.A. Karimi, G.A.T. Sevilla, A.M. Hussain, A. Shamim, M.M. Hussain, Paper skin multisensory platform for simultaneous environmental monitoring, Adv. Mater. Technol. 1 (2016), 1600004, https://doi.org/10.1002/admt.201600004.

[44] J. Wu, Z. Wu, K. Tao, C. Liu, B.R. Yang, X. Xie, X. Lu, Rapid-response, reversible and flexible humidity sensing platform using a hydrophobic and porous substrate, J. Mater. Chem. B 7 (2019) 2063–2073, https://doi.org/10.1039/c8tb02963f.

[45] M.U. Khan, G. Hassan, J. Bae, Bio-compatible organic humidity sensor based on natural inner egg shell membrane with multilayer crosslinked fiber structure, Sci. Rep. 9 (2019) 5824, https://doi.org/10.1038/s41598-019-42337-0.

[46] Y. Wang, L. Zhang, Z. Zhang, P. Sun, H. Chen, High-sensitivity wearable and flexible humidity sensor based on graphene oxide/non-woven fabric for respiration monitoring, Langmuir 36 (2020) 9443–9448, https://doi.org/10.1021/acs.langmuir.0c01315.

[47] Z. Duan, Q. Zhao, S. Wang, Z. Yuan, Y. Zhang, X. Li, Y. Wu, Y. Jiang, H. Tai, Novel application of attapulgite on high performance and low-cost humidity sensors, Sensors Actuators B Chem. 305 (2020), 127534, https://doi.org/10.1016/j.snb.2019.127534.

[48] Z. Duan, Q. Zhao, S. Wang, Q. Huang, Z. Yuan, Y. Zhang, Y. Jiang, H. Tai, Halloysite nanotubes: natural, environmental-friendly and low-cost nanomaterials for high-performance humidity sensor, Sensors Actuat. B Chem. 317 (2020), 128204, https://doi.org/10.1016/j.snb.2020.128204.

[49] Z. Duan, Y. Jiang, Q. Zhao, S. Wang, Z. Yuan, Y. Zhang, B. Liu, H. Tai, Facile and low-cost fabrication of a humidity sensor using naturally available sepiolite nanofibers, Nanotechnology 31 (2020), 355501, https://doi.org/10.1088/1361-6528/ab932c.

[50] Y. Zheng, L. Wang, L. Zhao, D. Wang, H. Xu, K. Wang, W. Han, A flexible humidity sensor based on natural biocompatible silk fibroin films, Adv. Mater. Technol. 6 (2021), 2001053, https://doi.org/10.1002/admt.202001053.

[51] S. Hou, Y. Shen, Y. Wang, X. Zhang, W. Luo, J. Huang, Ingestible, biofriendly, and flexible flour-based humidity sensors with a wide sensing range, ACS Appl. Electron. Mater. 3 (2021) 2798–2806, https://doi.org/10.1021/acsaelm.1c00372.

[52] Y. Shen, S. Hou, D. Hao, X. Zhang, Y. Lu, G. Zu, J. Huang, Food-based highly sensitive capacitive humidity sensors by inkjet printing for human body monitoring, ACS Appl. Electron. Mater. 3 (2021) 4081–4090, https://doi.org/10.1021/acsaelm.1c00570.

[53] S.P. Whelan, Z. Tehrani, M. Peacock, J.V. Paulin, O. Guy, D. Gethin, Investigation into the Suitability of screen printed graphene-melanin ph sensors for use in bacterial culturing applications, J. Electroanal. Chem. 904 (2022), 115868, https://doi.org/10.1016/j.jelechem.2021.115868.

[54] A.B. Mostert, K.J.P. Davy, J.L. Ruggles, B.J. Powell, I.R. Gentle, P. Meredith, Gaseous adsorption in melanins: hydrophilic biomacromolecules with high electrical conductivities, Langmuir 26 (2010) 412–416, https://doi.org/10.1021/la901290f.

[55] T.F. Wu, B.H. Wee, J.D. Hong, An ultrasensitive and fast moisture sensor based on self-assembled dopamine-melanin thin films, Adv. Mater. Interfaces 2 (2015) 1–5.

[56] L. Lu, C. Jiang, G. Hu, J. Liu, B. Yang, Flexible noncontact sensing for human–machine interaction, Adv. Mater. 33 (2021), 2100218, https://doi.org/10.1002/adma.202100218.

[57] B. Nie, R. Huang, T. Yao, Y. Zhang, Y. Miao, C. Liu, J. Liu, X. Chen, Textile-based wireless pressure sensor array for human-interactive sensing, Adv. Funct. Mater. 29 (2019), 1808786, https://doi.org/10.1002/adfm.201808786.

[58] S. Chun, W. Son, H. Kim, S.K. Lim, C. Pang, C. Choi, Self-powered pressure- and vibration-sensitive tactile sensors for learning technique-based neural finger skin, Nano Lett. 19 (2019) 3305–3312, https://doi.org/10.1021/acs.nanolett.9b00922.

[59] Y. Ren, Z. Liu, G. Jin, M. Yang, Y. Shao, W. Li, Y. Wu, L. Liu, F. Yan, Electric-field-induced gradient ionogels for highly sensitive, broad-range-response, and freeze/heat-resistant ionic fingers, Adv. Mater. 33 (2021), 2008486, https://doi.org/10.1002/adma.202008486.

[60] G. Wang, L.Q. Tao, Z. Peng, C. Zhu, H. Sun, S. Zou, T. Li, P. Wang, X. Chen, T.L. Ren, Nomex paper-based double-sided laser-induced graphene for multifunctional human-machine interface, Carbon NY. 193 (2022) 68–76, https://doi.org/10.1016/j.carbon.2022.03.026.

[61] Q. Hua, J. Sun, H. Liu, R. Bao, R. Yu, J. Zhai, C. Pan, Z.L. Wang, Skin-inspired highly stretchable and conformable matrix networks for multifunctional sensing, Nat. Commun. 9 (2018) 244, https://doi.org/10.1038/s41467-017-02685-9.

[62] R. Min, X. Hu, L. Pereira, M. Simone Soares, L.C.B. Silva, G. Wang, L. Martins, H. Qu, P. Antunes, C. Marques, X. Li, Polymer optical fiber for monitoring human physiological and body function: a comprehensive review on mechanisms, materials, and applications, Opt. Laser Technol. 147 (2022), 107626, https://doi.org/10.1016/j.optlastec.2021.107626.

[63] Z. Duan, Y. Jiang, H. Tai, Recent advances in humidity sensors for human body related humidity detection, J. Mater. Chem. C. 9 (2021) 14963–14980, https://doi.org/10.1039/d1tc04180k.

[64] W. Li, K. Ke, J. Jia, X. Pu, X. Zhao, R. Bao, Z. Liu, L. Bai, K. Zhang, M. Yang, W. Yang, Recent advances in multiresponsive flexible sensors towards e-skin: a delicate design for versatile sensing, Small (2021), 2103734, https://doi.org/10.1002/smll.202103734.

[65] S. Yoon, H. Yoon, M.A. Zahed, C. Park, D. Kim, J.Y. Park, Multifunctional hybrid skin patch for wearable smart healthcare applications, Biosens. Bioelectron. 196 (2022), 113685, https://doi.org/10.1016/j.bios.2021.113685.

[66] S.H. Chang, J.J. Huang, Biodegradability and anticoagulant properties of chitosan and sulfonated chitosan films coated on TiNi alloys, Surf. Coatings Technol. 206 (2012) 4959–4963, https://doi.org/10.1016/j.surfcoat.2012.05.121.

[67] N. Sadeghi, K. Shayesteh, S. Lotfiman, Effect of modified lignin sulfonate on controlled-release urea in soil, J. Polym. Environ. 25 (2017) 792–799, https://doi.org/10.1007/s10924-016-0848-6.

[68] S. Lee, Y. Hong, B.S. Shim, Biodegradable PEDOT:PSS/clay composites for multifunctional green-electronic materials, Adv. Sustain. Syst. 6 (2022), 2100056, https://doi.org/10.1002/adsu.202100056.

[69] H. Jin, Y.S. Abu-Raya, H. Haick, Advanced materials for health monitoring with skin-based wearable devices, Adv. Healthc. Mater. 6 (2017), 1700024, https://doi.org/10.1002/adhm.201700024.

[70] W. Wu, H. Haick, Materials and wearable devices for autonomous monitoring of physiological markers, Adv. Mater. 30 (2018), 1705024, https://doi.org/10.1002/adma.201705024.

[71] L.A. Schneider, A. Korber, S. Grabbe, J. Dissemond, Influence of pH on wound-healing: a new perspective for wound-therapy? Arch. Dermatol. Res. 298 (2007) 413–420, https://doi.org/10.1007/s00403-006-0713-x.

[72] P. Salvo, V. Dini, F. Di Francesco, M. Romanelli, The role of biomedical sensors in wound healing, Wound Med. 8 (2015) 15–18, https://doi.org/10.1016/j.wndm.2015.03.007.

[73] R.G. Frykberg, J. Banks, Challenges in the treatment of chronic wounds, Adv. Wound Care. 4 (2015) 560–582, https://doi.org/10.1089/wound.2015.0635.

[74] F. Mariani, M. Serafini, I. Gualandi, D. Arcangeli, F. Decataldo, L. Possanzini, M. Tessarolo, D. Tonelli, B. Fraboni, E. Scavetta, Advanced wound dressing for real-time pH monitoring, ACS Sensors 6 (2021) 2366–2377, https://doi.org/10.1021/acssensors.1c00552.

[75] Y. Li, Y. Wang, S. Chen, Z. Wang, L. Feng, Inkjet-printed paper-based sensor array for highly accurate pH sensing, Anal. Chim. Acta. 1154 (2021), 338275, https://doi.org/10.1016/j.aca.2021.338275.

[76] N.B. Guerra, G. Sant'Ana Pegorin, M.H. Boratto, N.R. de Barros, C.F. de Oliveira Graeff, R.D. Herculano, Biomedical applications of natural rubber latex from the rubber tree Hevea brasiliensis, Mater. Sci. Eng. C Mater. Biol. Appl. 126 (2021) 112126. 10.1016/j.msec.2021.112126.

[77] L.P. da Silva, S. Oliveira, R.P. Pirraco, T.C. Santos, R.L. Reis, A.P. Marques, V.M. Correlo, Eumelanin-releasing spongy-like hydrogels for skin re-epithelialization purposes, Biomed. Mater. 12 (2017), 025010, https://doi.org/10.1088/1748-605X/aa5f79.

[78] Z. Lin, L. Liu, W. Wang, L. Jia, Y. Shen, X. Zhang, D. Ge, W. Shi, Y. Sun, The role and mechanism of polydopamine and cuttlefish ink melanin carrying copper ion nanoparticles in antibacterial properties and promoting wound healing, Biomater. Sci. 9 (2021) 5951–5964, https://doi.org/10.1039/d1bm00622c.